Available online at www.sciencedirect.com

SCIENCE DIRECT®

Combustion and Flame 145 (2006) 339–356

Combustion and Flame

www.elsevier.com/locate/combustflame

Physical characterization of laminar spray flames in the pressure range 0.1–0.9 MPa

Stefano Russo, Alessandro Gomez [*]

Yale Center for Combustion Studies, Department of Mechanical Engineering, Yale University, P.O. Box 208286, New Haven, CT 06520-8286, USA

Received 7 February 2005; received in revised form 3 October 2005; accepted 5 October 2005

Abstract

An experimental study is reported on the physical characterization of the structure of ethanol/argon/oxygen coflow laminar spray diffusion flames in the pressure range 0.1–0.9 MPa. Diagnostic techniques include phase Doppler anemometry to measure the droplet size distribution and the axial and radial velocity components of the droplets. The gas-phase velocity is determined using measurements from the smallest (low Stokes number) droplets and is corrected for thermophoretic effects. Temperature information is obtained using thin-film pyrometry combined with an infrared camera. All flames present a cold inner core, in which little or no vaporization takes place, surrounded by an envelope flame buried in a thermal boundary layer, where most of the droplet evaporation occurs. The thickness of this thermal boundary layer scales with the inverse of the Peclet number. Especially near the base of the flame, photographic evidence of streaks, which in some case even reveal the presence of soot, suggests that some droplets survive the common envelope flame and burn isolated on the oxidizer side in a mixed regime of internal/external group combustion. The reconstruction of the entire droplet vaporization history confirms this evidence quantitatively. A criterion for droplet survival beyond the envelope flame based on the critical value of a suitably defined vaporization Damköhler number is proposed. The scaling and self-similar behavior of the investigated flames suggest that a mixed regime is established, with a momentum-controlled cold core and a buoyancy-controlled high-temperature boundary layer, the thickness of which varies significantly with pressure, as expected from Peclet number scaling. The growth of this layer and the thickness of the vaporization region are reduced at pressures above atmospheric because of density effects on thermal diffusivity. Some aspects of the design of the combustion chamber and of the atomizer system are discussed in detail since they are critical to the suppression of instabilities and to the establishment of a well-defined high-pressure quasi-steady laminar environment.

Keywords: Spray; Pressure; Laminar; Flame

1. Introduction

In many liquid-fuel applications, the gas in the combusting chamber is at pressures well above the atmospheric and in some cases it can reach conditions that are supercritical for the injected liquid fuels [1]. Not much has been reported to date on high-

---

[*] Corresponding author. Fax: +1 203 432 7654.
E-mail address: alessandro.gomez@yale.edu (A. Gomez).

doi:10.1016/j.combustflame.2005.10.002

pressure laminar spray flames, which are more complex than individual droplet burning, yet much better defined than practical spray systems. A study of such flames can help understand the basic phenomenology of high-pressure spray combustion. The surprising paucity of studies on this topic can be partially attributed to the inherent difficulties in setting up simple, small-scale, well-controlled experimental systems.

Laminar spray diffusion flames have been studied in both counterflow [2] and coflow [3] configurations at atmospheric pressure. Despite its intrinsic two-dimensional nature, the coflow configuration is, perhaps, better suited for high-pressure studies, since, unlike the counterflow case, most of the liquid phase evaporates and ultimately burns. It is also closer to the reactant injection pattern in practical configurations and can provide a fundamental understanding of practically relevant combustion regimes. Among the attainable regimes, group combustion [4], in which droplets burn collectively as a group rather than individually, prevails in spray flames, with the large majority of droplets vaporizing completely before reaching the reacting layer. Even in this pseudo-gaseous diffusion flame regime there may be droplets the residence time of which in the flame is smaller than the vaporization time. These droplets can survive the interaction with the flame, burn on the outside, and extinguish when a critical diameter is reached, in a combustion regime referred to as internal group combustion [5]. These isolated droplets may contribute to low combustion efficiency and NO_x production [6].

The goal of the present investigation is to examine the behavior of laminar spray flames spanning one order of magnitude in pressure, yet far removed from the complexities of critical phenomena. After describing the experimental apparatus and the quantitative and qualitative criteria used to design it, we examine the physical structure of these flames and the effects of a ninefold change in pressure on their scaling and self-similar behavior. Particular attention is devoted to the vaporization history of droplets that do not fully vaporize before reaching the diffusion flame in a regime of internal group combustion. Results on two of the four flames studied were presented in [7].

2. Experimental system, design consideration, and test conditions

2.1. The chamber

The design of the vessel to perform high-pressure combustion experiments is a rather complex task and requires meticulous attention to details. Optical access, safety, proper fluid dynamic behavior, and mechanical strength are all essential characteristics, the importance of which should not be underestimated. We give below an extensive description of the criteria followed in the design of the system, since they proved to be a major challenge in the initial phase of the project. A sketch of the complete experimental apparatus used in the high-pressure spray combustion experiment is shown in Fig. 1a. The chamber, with inner diameter measuring 8.25 cm, was designed with three openings to provide optical access to the reacting flow under investigation. BK7 glass was used for phase Doppler measurements, while for temperature measurements one of the glass windows was replaced with a zinc–selenide one with high infrared transmissivity. To improve the S/N ratio of the phase Doppler signal, a 68° angle between windows was chosen to approach the Brewster angle for scattering from ethanol droplets. The optically accessible section was positioned to have the bottom of the windows at the same height as the burner outlet. Because of the limited optical accessibility of the chamber, it was possible to scan only the first 20 mm of the four flames. It will be shown later that this area is the most interesting from the point of view of group combustion and is relatively immune from buoyancy-induced instabilities that invariably set in further downstream in the flame.

The structure of the diffusion flame is strongly influenced by the fluid dynamic characteristics of the combusting flows. In designing the chamber, special care had to be taken to avoid external, chamber-induced, fluid-dynamic effects influencing the reacting flow. To that end, a chamber extension was mounted at the top of the optically accessible section to damp fluctuations associated with buoyancy induced instabilities and expand the pressure range over which quasi-steady behavior could be established. The chamber was equipped with typical safety features such as burst disks and pressure release valves. Pressure was regulated using a valve throttling the exhaust. Further details, with remarks on an acoustic analogy that helped us size the chamber up, are given in Appendix A and in [8].

2.2. Liquid supply system

The atomizer was mounted at the base of the high-pressure stainless steel chamber. For the high-pressure spray flames under investigation the atomizer selection proved to be critical since such flames are very sensitive to the specific atomization technique. Pressure atomizers [2] are not well suited to this function since they do not offer good control over the size distribution and their adaptation to laminar spray flames requires sufficient time for the two

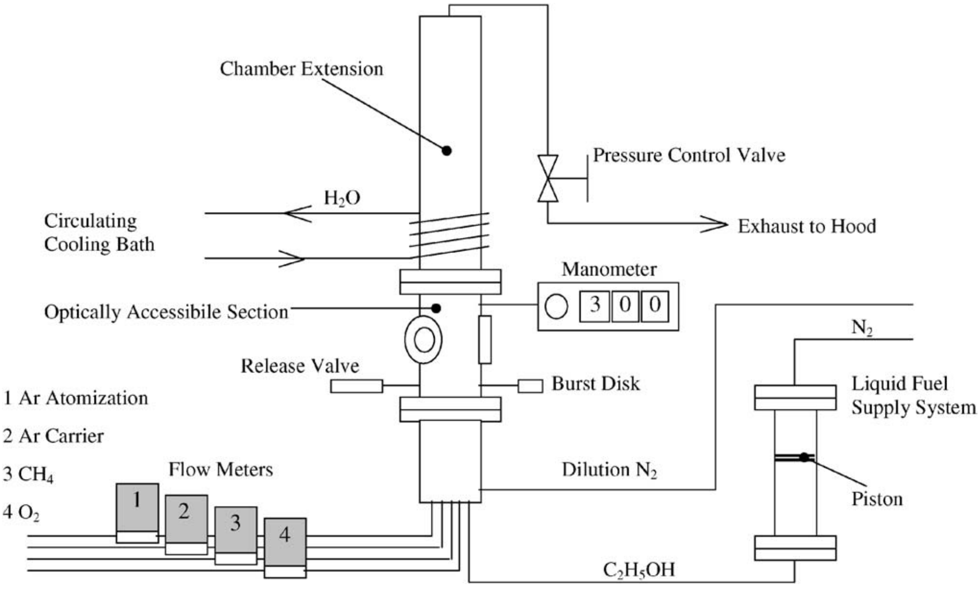

(a)

Fig. 1. (a) Experimental apparatus; (b) burner and atomizer details.

phases to equilibrate in a large settling chamber. The last requirement conflicts with the need to keep at a minimum the volume of such a chamber to avoid buoyancy-induced instabilities at high pressures, as explained in Appendix A. Ultrasonic atomizers [9, 10] are also inappropriate, as we discovered in preliminary experiments, since the pressure waves generated during the atomization process introduce strong disturbances in the flame as the pressure increases above one atm. By a process of elimination, the best compromise spray system that satisfied all the necessary prerequisites turned out to be a homemade spray generator (inset in Fig. 1b) that was based on the laminar aerodynamic shearing of a liquid jet by a gaseous coflow [11]. Its operating principle is as follows. A small hole in a thin plate through which a gas stream is flowing generates velocity and pressure fields with relatively strong gradients next to the aperture. If the meniscus at the tip of a capillary tube is inserted in the pressure field coaxially to the small hole, the liquid elongates towards the opening. When the pressure drop through the hole overcomes the liquid–gas surface tension stresses, the meniscus develops in a cusp-like shape. If a constant liquid-flow rate is supplied through the capillary, a steady thin liquid jet is emitted. After exiting the hole, the jet diameter remains almost constant up to the point where the jet breaks up because of capillary instabilities in the so-called Rayleigh break-up regime. The generated spray is expected to produce droplets of uniform size as long as the gaseous flow is laminar. This constraint limits the maximum allowable liquid flow rate for a fixed droplet size.

To overcome this limitation the atomizer had to be multiplexed. Two different configurations were adopted. The first one with three capillary tubes reached a maximum flow rate of 0.7 ml/min. In the second one, nine capillary tubes had to be positioned in parallel to reach a total flow rate of 2.1 ml/min with a flow rate per tube of approximately 0.23 ml/min. After a few iterations, a diameter of 75 µm was chosen for each hole. Each hole was positioned in the plate with a precision of ±5 µm to ensure coaxiality with the 400-µm o.d. tubes. A further decrease in size of the hole would have brought excessive complications in the control of the relative position between the holes and the tubes. The tubes were held in place by two 12-mm thick Teflon disks, kept at a distance of 20 mm by threaded rods. A sketch of the atomizer is visible in the inset of Fig. 1b.

Contrary to the claims in [11], monodispersity was never reached, possibly because of various limitations in the adjustment of the atomizer. However, a modest level of polydispersion, as the one achieved in the present design, turned out to be beneficial, since the small droplets were useful to ensure flame stabilization, whereas the larger ones would survive the diffusion flame and burn on the outside, mimicking the behavior of practical sprays. Furthermore, the atomizer allowed for some level of manipulation of the distribution, with the possibility of tracking the vaporization of droplets in deliberately produced spikes in the distribution.

The liquid fuel was fed into the atomizer from a container pressurized with nitrogen. The flow rate was controlled by changing the stagnation pressure in the

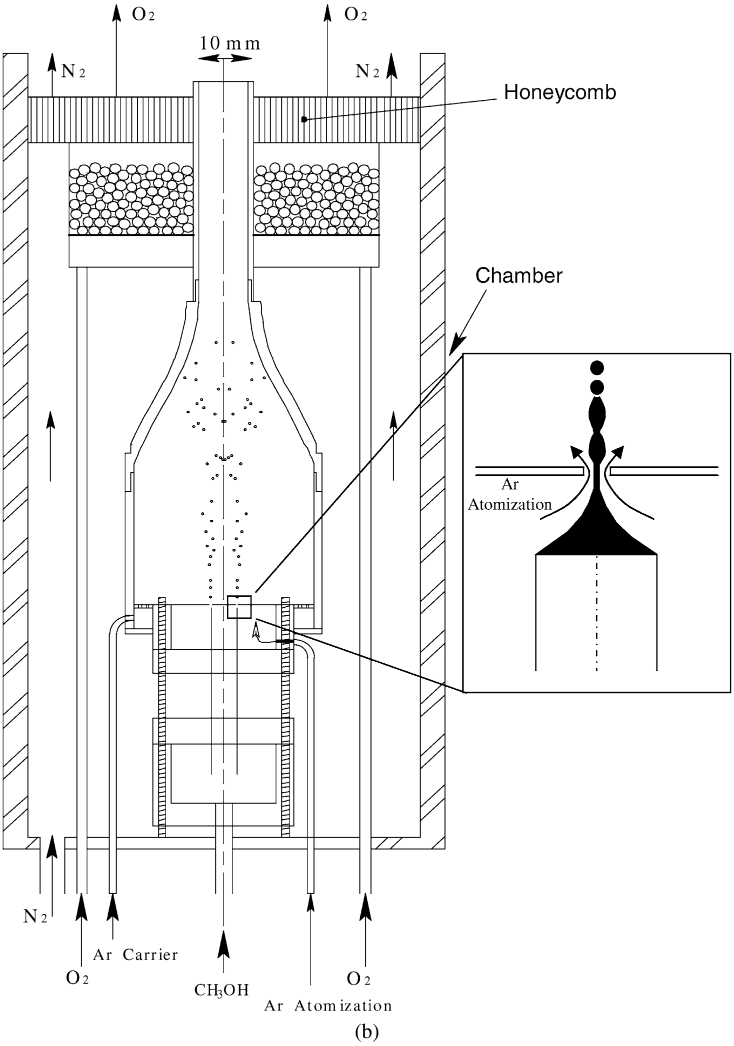

Fig. 1. Continued.

vessel. Contact between the two phases was avoided, to prevent dissolution of the pressurizing gas into the liquid and, ultimately, the formation of bubbles in the delivery line. To that end, as shown in Fig. 1a, a piston with tight tolerances was designed so that it would be capable of moving freely into the cylinder but avoided the direct contact between the liquid and the gas. To monitor the liquid level in the vessel a small magnetic element was mounted on the piston. Another magnet was placed on the outer wall of the vessel and moved along the surface of the tank with the piston via magnetic field coupling.

2.3. *Test conditions and characteristic numbers*

Argon was used as a carrier gas entering the chamber on the side of the atomizer and carrying the spray upward through a 30° contraction terminating in a 7.5-cm-long tube with an inner diameter of 10 mm. Two different reasons motivated the selection of argon as the inert, as opposed to either nitrogen or helium: it has a molar heat capacity smaller than that of nitrogen, resulting in higher flame temperatures, which helps stabilizing the flame; it has a density larger than that of helium, which helps counteract buoyancy. Ethanol was selected as a fuel because of its low sooting tendency.

Liquid fuel from droplets that impinged on the walls of the atomizer was collected at the base of the duct in a deep groove on the side of the atomizer. The carrier gas bubbled through it and carried it downstream in the form of vapor. As a result, no significant accumulation of liquid was observed during the experiments. At the exit of the duct, the droplet-laden jet met with a pure oxygen stream with a constant inlet velocity ≈4.5 cm/s and burned in a coflow

Table 1
Physical parameters for the four flames

Flame	Pressure (MPa)	C_2H_3OH (ml/min)	Ar (slpm)	CH_4 (slpm)	T_{ad} (K)	U_{avg} (m/s)	ν [300 K] (m^2/s)	α [300 K] (m^2/s)	t_0 (mm)
1	0.1	0.7	2.7	0.018	2549	0.58	13.9×10^{-6}	20.9×10^{-6}	2.0
2	0.3	0.7	2.7	0.034	2683	0.19	4.6×10^{-6}	7.0×10^{-6}	1.4
3	0.3	2.1	8.1	0.115	2634	0.58	4.6×10^{-6}	7.0×10^{-6}	1.1
4	0.9	2.1	8.1	0.155	2719	0.19	1.5×10^{-6}	2.3×10^{-6}	0.7

diffusion flame. A system of screens, packed glass beads, and honeycomb (Fig. 1b) guaranteed the laminarity of the oxidizer coflow. The burner was positioned at the base of the high-pressure combustion chamber and kept in place by applying suitable tension to the connected gas tubes. A nitrogen shroud flow was supplied at the base of the chamber on the outside of the burner to prevent recirculation of the gases above the honeycomb and to keep the windows clean from any kind of vapor or particulate deposit.

Table 1 gives a summary of the examined flame conditions, listing flow rates of fuel and inert, adiabatic flame temperatures, the axial component of the average velocity in the fuel stream, the inert momentum and thermal diffusivities. Four flames were investigated, with the fuel to inert ratio kept constant in all four cases. In Flame 1 and Flame 2, 0.7 ml/min of ethanol where injected into 2.7 slpm of argon at 0.1 MPa and 0.3 MPa, respectively. Flame 3 and Flame 4 were established with 2.1 ml/min of ethanol and 8.1 slpm of argon at 0.3 MPa and 0.9 MPa, respectively.

To ensure the attachment of the flame at the tip of the fuel tube, some methane had to be added to the fuel side. Since the focus of the present investigation is on the physical structure of the flames, it was easier to hybridize the fuel stream with the addition of a gaseous hydrocarbon, rather than alcohol vapor. Notice that in any spray flames the coexistence of fuel in both the liquid phase and the gaseous phase is inevitable and their relative amounts decreases in the streamwise direction. In this sense, the deliberate addition of gaseous fuel in the feed stream is tantamount to mimicking conditions that would inevitably prevail somewhere downstream of the injector in a pure spray flame. Methane provided approximately 4% of the total enthalpy for Flame 1, 8% for Flames 2 and 3, and 10% for the flame at the highest pressure. Adiabatic flame temperature calculations took into account the gaseous hydrocarbon addition.

Some estimates of overall nondimensional parameters may be helpful in establishing similarities and differences among the flames. The characteristic numbers relevant to the present problem are the Reynolds, Peclet, and Richardson numbers, defined as $\mathrm{Re} = \frac{U_{avg}R}{\nu}$, $\mathrm{Pe_h} = \frac{U_{avg}R}{\alpha}$, $\mathrm{Ri} = \frac{\Delta\rho}{\rho}\frac{gR}{U_{avg}^2}$, respectively, with R as the burner mouth radius, U_{avg} as the average velocity at the burner mouth, ν and α as the momentum diffusivity and the thermal diffusivity, g as the gravitational acceleration, and ρ as the density.

Table 2
Characteristic nondimensional numbers for the four flames

Flame	Pressure (MPa)	Re	$\mathrm{Pe_h}$	Pr	Ri
1	0.1	200	135	0.67	0.4
2	0.3	200	135	0.67	3.7
3	0.3	600	400	0.67	0.4
4	0.9	600	400	0.67	3.7

The conditions described in Table 1 were chosen so that the values of these numbers reported in Table 2 would be reached, with transport properties calculated at 300 K for pure argon. Buoyant forces were assumed as generated by an average temperature difference of 1400 K. A careful selection of flow conditions was in principle tuned toward isolating individual effects in the four flames. For example, Flames 1 and 3, as well as Flames 2 and 4, have the same Richardson number, which should result in a similar buoyant behavior. On the other hand, Flame 1 has the same Peclet number as Flame 2, which should result in a similar temperature field. Clearly, these considerations only apply in an overall sense. Further details on scaling and self-similarity, as well as their controlling parameters will be given in the discussion of the results. The present set of measurements broadens considerable the pressure range and the Richardson number range, as compared to our earlier work discussing only Flames 1 and 3 [7].

2.4. Diagnostics

The distributions of droplet size, together with the axial and radial velocity components were measured using phase Doppler anemometry (Dantec Elektronik). All the flames presented a number of droplets below 10 μm in size that, under the present conditions, had Stokes number lower than 2×10^{-2} and, in the region of largest radial velocity gradient, less than 7×10^{-2}. Therefore, they can be considered good trackers of the gas, if thermophoretic effects are properly accounted for.

Gaseous temperatures between 900 and 2200 K were measured via silica-carbide thin filament pyrometry [12] using an infrared camera (Electrophysic Corp. PV320) with a 50-mm germanium lens. The camera response was calibrated using a thermocouple in a heated stream.

3. Results and discussion

3.1. Flame appearance

As shown in the pictures in Fig. 2, the first two or three flames had the typical quasi-conical appearance of gaseous flames, with the fourth flame being nearly cylindrical in the lower section that was optically accessible in this study. The striking difference from strictly gaseous flames was the appearance of luminous, in the last case sooty, streaks provisionally associated with droplets punching through the common gaseous flame enveloping the bulk of the spray. As shown below, detailed measurements of droplet size and velocity and flame temperature provided quantitative evidence corroborating this interpretation. The extent of this mixed combustion mode, typically defined as internal group combustion [5], varied from flame to flame, with the most pronounced "streaking" in Flame 4 and the least pronounced in Flame 2. The streaks appeared more frequently near the anchoring region at the flame base.

Flame 1, at atmospheric pressure, exhibited a steady, blue, reacting layer measuring approximately 45 mm in height (grayish quasi-vertical line in Fig. 2a). Flame 2 was also stable and measured only 30 mm in the vertical direction (Fig. 2b). Flame 3 exhibited instabilities in the upper part in the way of flickering that is typically associated with buoyancy effects [13,14] (Fig. 2c). These fluctuations did not have a significant effect on the lower part of the flame. The maximum axial amplitude of the oscillation was reached at approximately 45–50 mm well above the section under consideration in this study. At 20 mm the flame oscillated radially only ±0.25 mm around its average diameter of 9.60 mm with a ∼12 Hz frequency as recorded by temperature measurements. Because of the low tendency of ethanol to soot and of the high dilution, no yellow emission from carbon particles was recorded in any of the first three cases. Soot volume fraction is known to scale linearly with pressure in the combustion of fuel droplets in high-pressure gaseous environments [15]. In fact, some of the droplets escaping the diffusion flame at the highest pressure in Flame 4 did produce soot, as can be seen in Fig. 2d. The yellow spots were caused by blackbody emission from soot created by envelope flames surrounding the droplets that exited the flame and burned on the outside. Near the anchoring point, the number of droplets exiting the diffusion flame reached a maximum, but differently from the previous cases, streaks of droplets burning in envelope flames could be seen also higher up in the axial direction. At approximately 16 mm, instabilities started to develop. Also, in this case the source of instabilities has to be attributed to the buoyant acceleration of the hot gases [16]. Flames 2 and 4, because of low inertia, were subject to the strongest buoyancy influence. While the low Reynolds number and the relatively small height of Flame 2 did not allow instabilities to develop, in Flame 4 the fluctuations were significant and the reacting layer became unstable well below 20 mm.

3.2. Key features of the droplet size distributions

In principle, droplet size distributions with some common features in all four flames would be desirable for ease of comparison. For example, if the cumulative volume distribution of the droplets, indicating the percentage of the total liquid volume contained in

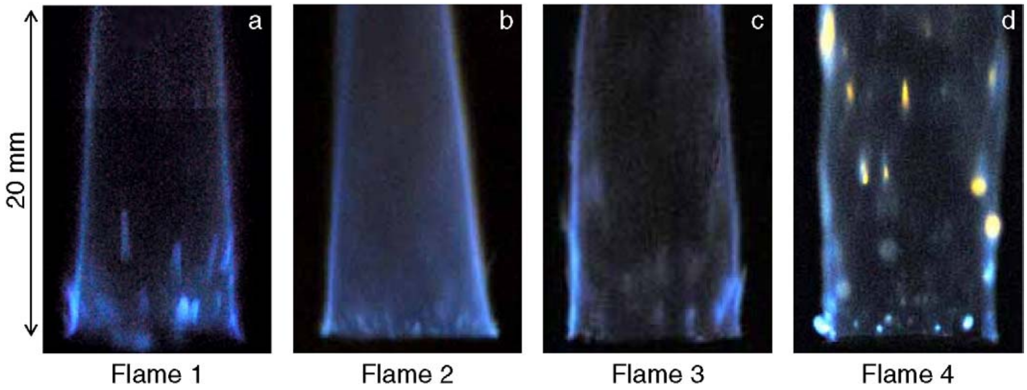

Fig. 2. (a–d) Chemiluminescence image for Flames 1–4. In all the flames individual droplets burning are visible. In (d), corresponding to Flame 4, some local soot production and ensuing blackbody emission is also visible.

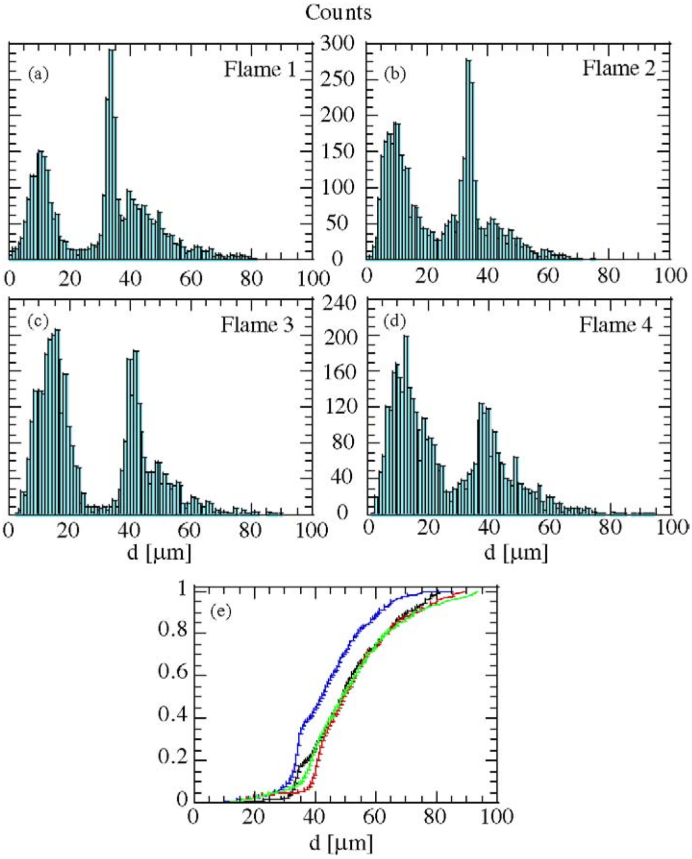

Fig. 3. (a–d) Droplet size distribution for Flames 1–4 at $r = 0$ and $z = 0.75$ mm; (e) cumulative volume distribution for the different flames.

all droplets with diameter less or equal than a specified value, were approximately the same, any sharp difference in evaporation history could be attributed to different temperature–time histories. Similarly, the presence of sharp peaks in the size distribution may offer the opportunity to track the evaporation of subsets of droplets experimentally. With this in mind, by manually adjusting the axial distance of the needles relative to the perforated plate, we tweaked the atomizer configuration till typical distributions at the exit of the burner appeared as in Figs. 3a–3d. In Flame 1, a strong peak around 33 µm, corresponding to the main mode of Rayleigh break-up of the liquid filament, is clearly visible. A smaller peak around 40 µm corresponds to the second harmonic. Other modes of oscillation were buried in the remaining part of the distribution. Clearly visible are also satellites droplets produced during the atomization process and falling in the range 0–20 µm. Similar features were present also in the distribution of the high-pressure, low-flow-rate flame (Flame 2). While for Flames 1 and 2 the main peak was at 33 µm, for Flames 3 and 4 the main peak was located at around 40 µm and the second harmonic at 50 µm. The good correspondence between the distributions is shown in Fig. 3e, where the volume distributions are compared. Three curves, pertaining to Flames 1, 3, and 4, are almost superimposed, with small differences only in the range 33–40 µm, depending on the location of the main peak. Slightly different was the distribution for Flame 2, for which, because of the lack of droplets in the range 70–100 µm, the volume distribution was systematically above the others (leftmost curve). Those big droplets accounted only for approximately 10% of the total volume and the volume distribution of Flame 2 differed from the others by only about 15%. As a result, the goal of "shaping" distributions with some common features for ease of interpretation and for diagnostic purposes was achieved, although we never managed to operate the atomizer in the monodisperse mode, as reported in [11].

3.3. Gas velocity scaling and self-similar behavior

The axial "gaseous" velocity component, measured by tracking low-Stokes-number droplets, is shown in Figs. 4a–4d at selected axial locations in the first 20 mm of Flames 1–3 and in the first 16 mm of Flame 4. The arrow in the figures indicates the direction of increasing axial position. In all the figures, the right side corresponds to $\theta = 0$ and differs from the left part by π in polar coordinates.

All radial scans exhibited good cylindrical symmetry. At the burner mouth, Flame 1 had an almost parabolic axial velocity profile, which became progressively flatter in Flame 2, and even more so in Flames 3 and 4, characterized by a larger Re (see Table 2). Expectedly, all profiles were perturbed in the heat release region near the outer periphery of the scans, as a result of density changes and buoyancy acceleration. These perturbations became broader and broader higher up in the flame, as a result of the growth of the boundary layer at the interface of the fuel jet and the coflow oxygen.

Fig. 5a reports the measured axial component of the velocity along the centerline as a function of the axial coordinate. The velocity remained nearly constant or decreased for the four flames. This is a characteristic of momentum-controlled diffusion flames, unlike the typical $\sqrt{z}$ dependence of buoyancy-controlled flames [17]. Because of the low value of the Richardson number (see Table 2), inertia was dominant over the buoyant acceleration and the centerline velocity was not affected by buoyancy.

The value of the axial velocity at the location where the temperature peaked is shown in Fig. 5b as a function of the square root of the axial coordinate, under the premise that the scaling should follow

$$u(z) \approx \left[2\left(\frac{\Delta\rho}{\rho}\right)gz\right]^{0.5},$$

where $\Delta\rho/\rho$ is a density factor and g the gravitational acceleration. Flames 1 and 3 had a similar behavior, as did Flames 2 and 4. Because of the high temperature the density difference between these locations and the free stream was large and, locally, the flames were strongly affected by buoyancy. The ratio of buoyancy to inertia, the Richardson number, controlled the velocity behavior. Flames 1 and 3 had the same Ri (Table 2) and similar velocity behavior. An analogous trend can be seen for Flames 2 and 4. In all four cases above 4 mm ($z^{0.5} = 2$), the behavior was linear and with similar slopes. But, because of the higher inertia, Flames 1 and 3 still appeared to be momentum controlled at the lower heights and the velocity locally increased because of viscous effects and thermal expansion. A few millimeters downstream buoyancy set in, the velocity gradients decreased, buoyancy dominated over viscous forces and the slope of curves 1 and 3 approached the one for Flames 2 and 4.

A first conclusion on the structure of the flames can be drawn on the basis of the presented data. Differently from diffusion flames in air [18], these highly diluted diffusion flames were momentum-controlled in the center while presenting a buoyancy-controlled annulus on the outside. For flames at lower Ri, buoyancy "intervention" was delayed with respect to flames with higher buoyancy to inertia ratio. In the inner core, because of the unchanged temper-

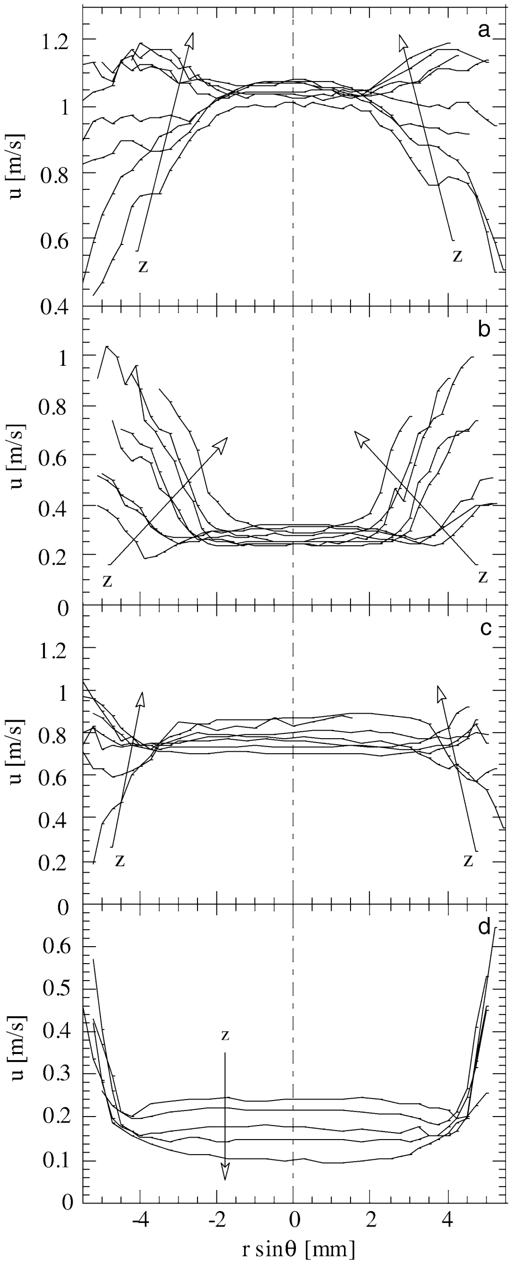

Fig. 4. Radial profiles of the axial velocity component at selected heights above the burner: (a) Flame 1 ($z = 0.75$, 2, 4, 7, 10, 12, 16, 18, 19.5 mm); (b) Flame 2 ($z = 0.75$, 2.5, 5, 10, 12, 16, 18, 20 mm); (c) Flame 3 ($z = 0.75$, 4, 5, 8, 12, 16, 18, 20 mm); (d) Flame 4 ($z = 0.75$, 4, 8, 12, 16 mm).

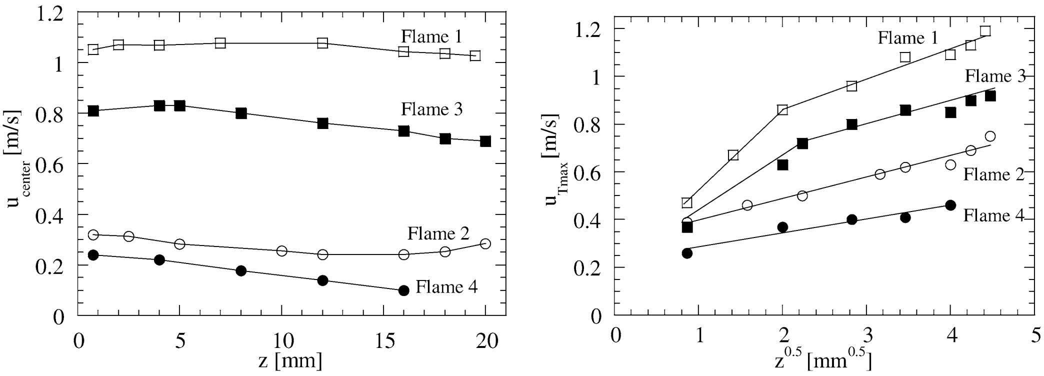

(a) (b)

Fig. 5. (a) Axial velocity component along the centerline as a function of height above the burner; (b) axial velocity component at the radial location of maximum temperature as a function of the square root of the height above the burner.

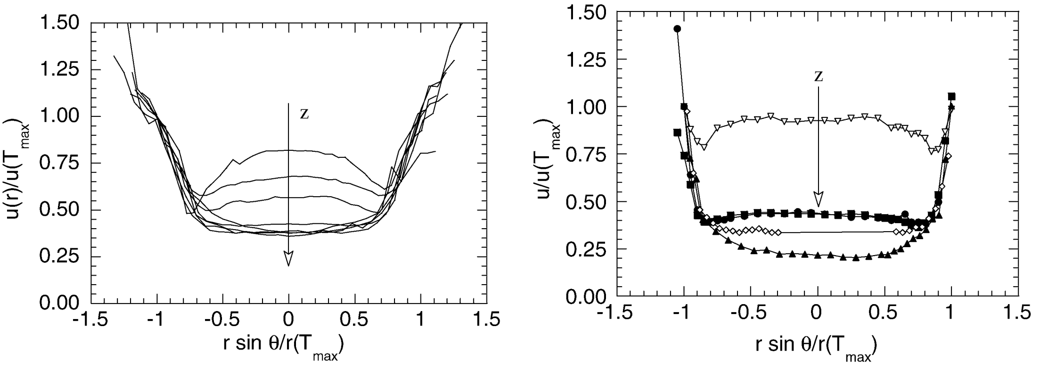

(a) (b)

Fig. 6. Axial velocity as a function of the radial position, both normalized with respect to the values at the point of maximum temperature; (a) Flame 2; (b) Flame 4.

ature, buoyant forces were absent and the velocity profile was controlled by the Reynolds number. In Flames 1 and 2 with equal Reynolds number, the velocity profiles were self similar (parabolic) in the central, cold, region with constant temperature. In Flames 3 and 4 the velocity profile was almost flat. Different was the behavior in the external layer. At increasing values of the radial coordinate, as the temperature increased, buoyancy competed with inertia and the Reynolds number based similarity was lost, while a Richardson number based similarity was attained (Fig. 5b) between Flames 1 and 3, and between Flames 2 and 4.

In Flames 2 and 4, because of the low velocity, buoyancy easily overcame inertia in the outer layer, the hot gases were strongly accelerated and the axial velocity maintained a self-similar behavior. Fig. 6a shows the axial velocity profile for Flame 2, normalized with respect to the axial velocity at the point of maximum temperature at the same height. The abscissa is the radial coordinate normalized with respect to the radial coordinate at the maximum temperature location. The self-similarity of the velocity profile is evident in the outer layer and at higher axial positions held also towards the center. Similar behavior was encountered in Flame 4, but in this case, because of the higher Peclet number, the hot region was narrower (Fig. 6b). As discussed earlier, because of the one order of magnitude difference in Richardson number, buoyancy played a different role in Flames 1 and 3. Since it competed with inertia in a mixed regime in which neither dominated, self-similarity was not established.

Radial velocity components of droplets smaller than 10 µm are reported in Figs. 7a–7d at selected axial locations in the first 20 mm of Flames 1–3 and in the first 16 mm of Flame 4. In all cases, the radial velocity presented a region of constant, almost zero velocity and external wings with nonzero gradients. Differently from the axial behavior, the droplets were moving in regions of strong temperature gradients in the radial direction and thermophoretic effects cannot be disregarded. In this case the gaseous velocity is the difference between the measured droplet velocity and

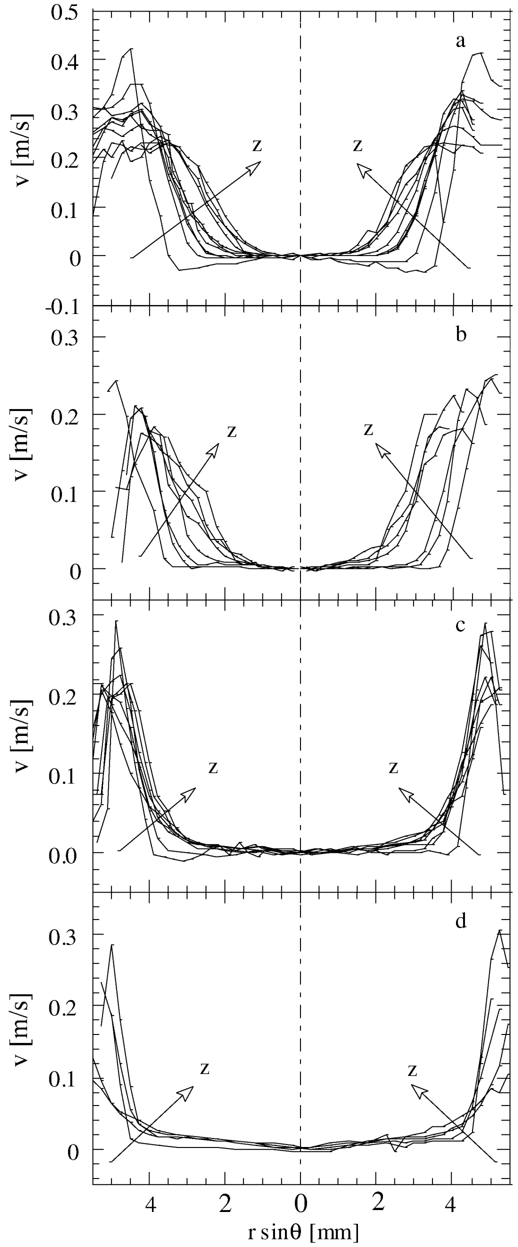

Fig. 7. (a–d) Radial profiles of the radial velocity component at selected heights above the burner for Flames 1–4.

the thermophoretic drift,

$$v_g = v - v_T,$$

where v_g is the radial gaseous velocity, v and v_T represent the droplet velocity and the thermophoretic drift, respectively. The local particle drift velocity can be defined as

$$v_T = -(\alpha_T D_p) \times \left(\frac{\bar{\nabla} T}{T}\right),$$

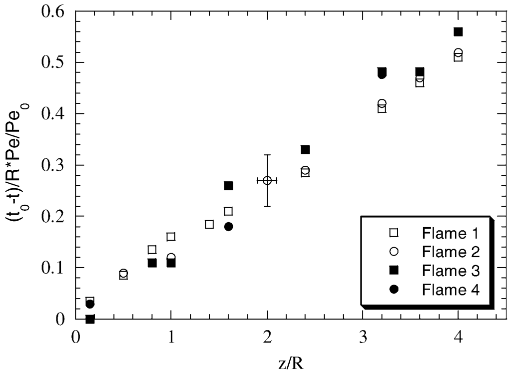

Fig. 8. Normalized axial growth of the thermal layer (t is the radial thickness of the cold region; t_0 is the extrapolated thickness at $z = 0$; Pe is the Peclet number in the cold region; Pe_0 is the Peclet number in the cold region of Flame 1).

where $(\alpha_T D_p)$ is the thermophoretic diffusivity resulting from the product of D_p, the particle Brownian diffusivity, and α_T, the dimensionless thermophoretic diffusion factor. To evaluate the diffusivity, use can be made of $\alpha_T D_p \approx 0.5\upsilon$, where υ is the gas momentum diffusivity [19]. In Flame 1, for the region of maximum temperature gradient (~1000 K/mm) and with transport properties evaluated at 1000 K, the thermophoretic drift was estimated to be on the order of 3 cm/s, which is not negligible when compared with the droplet velocities in this region. Smaller drift velocities were calculated for the other flames because of the pressure effect on the argon diffusivity dominating over the smaller increase in temperature gradient.

The evolution of the radial velocity profiles shows evidence of a cold core, in which little or no vaporization took place. In that region, the temperature remained constant since the flow had not been influenced yet by the flame generated heat. The dimension of the cold region can be inferred from droplet size or radial velocity measurements [7,8].

The radial growth of the thermal layer is related to the relative magnitude of convection and diffusion, i.e., the Peclet number. The normalized thickness of the thermal layer is reported in Fig. 8 as a function of a normalized axial coordinate. The ordinate is defined in terms of: t, the thickness of the cold region; t_0, the extrapolated thickness at $z = 0$ (listed in Table 1); Pe, the Peclet number in the cold region; and Pe_0, the Peclet number in the cold region of Flame 1. A ±0.25-mm error in measuring the thickness and a ±0.5-mm uncertainty in determining the height are represented by the error bars in the figure. Once corrected for Peclet number effects, the thermal layer had a similar growth in all four flames.

3.4. Determination of droplet trajectories and evaporation history

In Figs. 9a–9d we show the measured gas temperature for the four flames as a function of spatial coordinates. Thin filament pyrometry was applicable only above 900 K. The cold core temperature was measured at 288 K by a thermocouple for Flame 1 and assumed constant for the four flames [8]. In the remaining region we interpolated the temperature from 900 to 288 K with a Stineman function [20], smoothly matching the slope in the high-temperature region to the zero gradient in the cold core. The horizontal line in the figure shows the temperature upper boundary to the region where the interpolation procedure was applied. The same considerations that were made about the axial velocity profiles, with respect to the spread of the mixing layer and its scaling with Pe, apply obviously also to the thermal profiles. In each of the flames the peak temperature remained almost constant at different heights. Since pressure effects reduce molecular dissociation, higher values of the peak temperature were measured at high pressure [21].

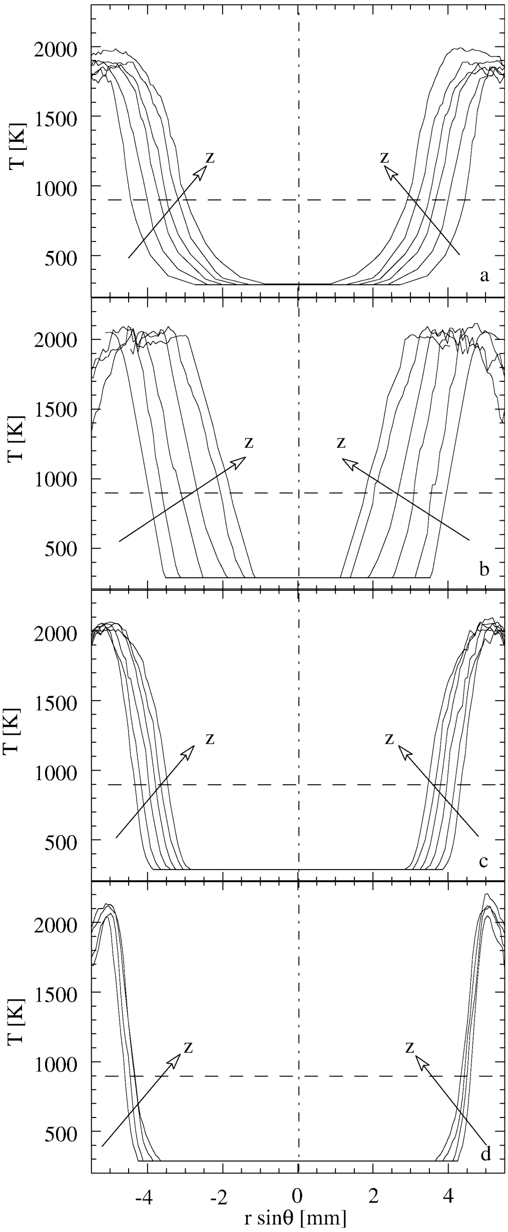

Fig. 9. Gaseous temperature as a function of the radial coordinate at selected heights ($z = 1$, 4, 8, 12, 16, 20 mm for Flames 1–3 and $z = 1$, 4, 8, 12, 16 mm in the case of Flame 4).

Capitalizing on the knowledge of temperature, velocity, and droplet size distribution at every point in the flow field, we can track the evolution of some of the modes of the distribution and verify if it is consistent with theory. Specifically, the evolution of the diameter of a single droplet vaporizing in a quiescent atmosphere can be followed by tentatively applying the d^2-law, that is,

$$-\frac{\mathrm{d}d^2}{\mathrm{d}t} = \frac{8\lambda}{\rho_1 C_\mathrm{p}} \ln\left[1 + \frac{C_\mathrm{p}(T_\infty - T_\mathrm{w})}{L}\right] = K. \qquad (1)$$

Implicit in the use of this formula is the negligibility of convective effects, since Reynolds numbers based on relative velocities were estimated to be on the order of 10^{-1}. Since the composition of the fuel stream was constant for the four flames at 10 mol of inert gas per mole of fuel, argon can be assumed as the only gaseous component. With a suitable choice of the droplet wall temperature T_w, the evaporation coefficient reduces to a mere function of the gas-phase temperature, $K(T)$. Once the gas-phase temperature is known, we can use Eq. (1) to follow the droplet size evolution in the flame. Notice, also, that only the first part of the droplet vaporization history is dependent on the particular technique used for temperature interpolation. For example, for the 40-μm droplet less than 10% of diameter decrease can be attributed to that part of the flame where the gaseous temperature is obtained via interpolation.

In Fig. 10a the evolution of droplet diameter in Flame 1 along a droplet trajectory is shown for three different droplets of initial sizes, 33, 40, and 60 μm. This figure is adapted from Ref. [7] for comparisons purpose. The trajectory is tracked by the axial coordinate in the abscissa. The droplets, despite starting from the same position ($r = 3.0$ mm and $z = 1.0$ mm), followed different trajectories as a result of different initial velocities and inertial behavior. The calculated size evolution, represented by the continuous lines following Eq. (1), is in good agreement with the experimentally measured one, repre-

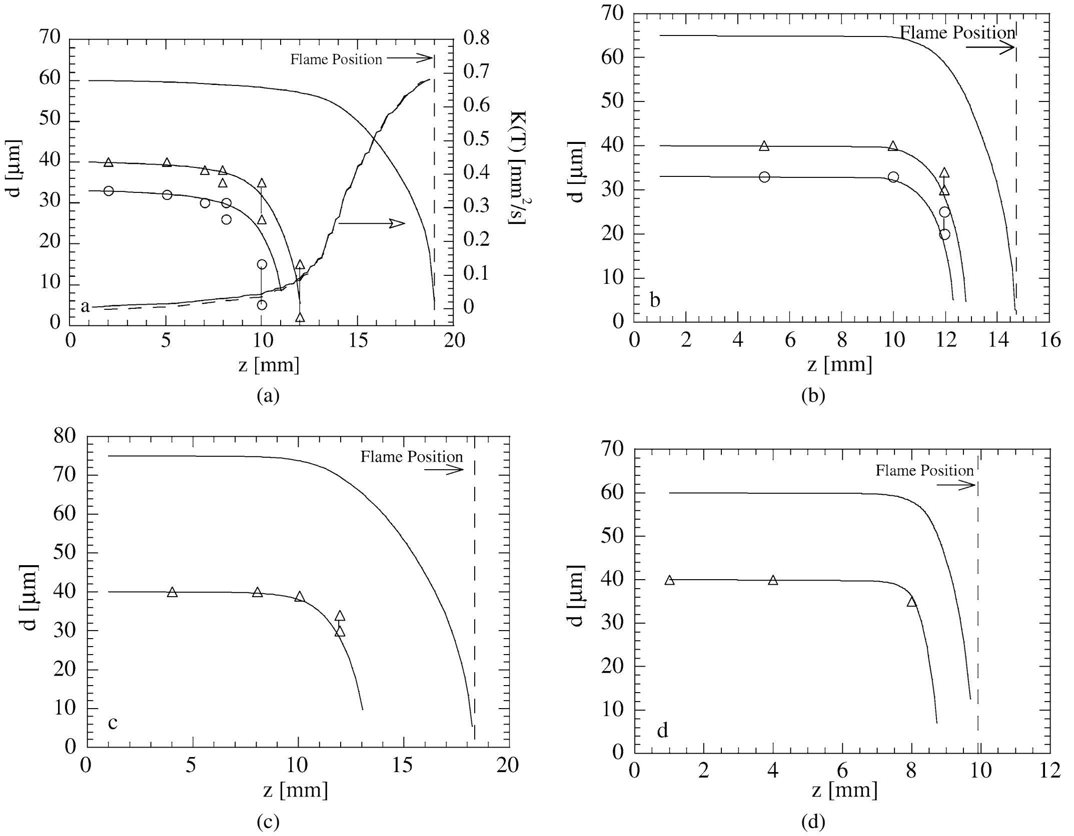

(a)

(b)

(c)

(d)

Fig. 10. (a) Flame 1. Left ordinate: droplet size history as a function of the vertical coordinate for three different initial sizes: 33, 40, and 60 μm. Continuous lines are computed; open circles and triangles are the experimental data. Right ordinate: evaporation coefficient for the 60-μm droplet based on an assumed droplet wall temperature of either 288 K (continuous line) or 351 K (dashed line), respectively. The latter value is the ethanol boiling point. (b) Flame 2. Droplet size history as a function of the vertical coordinate for three different initial sizes: 33, 40, and 65 μm. (c) Flame 3. Droplet size history as a function of the vertical coordinate for two different initial sizes: 40 and 75 μm. (d) Flame 4. Droplet size history as a function of the vertical coordinate for two different initial sizes: 40 and 60 μm.

sented by the open symbols for both cases for which traceable modes of the initial distributions were available. If droplet size measurements were not available at the precise radial location, the two closest points are reported. The measured size is expected to be in the range represented by the bar connecting the two symbols. Similar results were obtained for the other flames. The comparisons, however, are less extensive because only one mode of the distribution could be used for evaporative tracking in Flames 3 and 4. Also, the high pressure flames, especially Flame 4, exhibited such a thin thermal layer, that the bulk of the droplet evaporation occurred in a very narrow region on the order of less than one or two mm thick. Nevertheless, the overall picture emerging from these data is undoubtedly that the classic d^2-law applied under the assumption that the droplet in the flame core evaporated in inert gas at the prevailing temperatures.

We can now confidently compute the size evolution of droplets of arbitrary size, despite the lack of detailed measurements that would require too great a manipulation of size distributions with sparse data in the distribution "tails." This is shown with the continuous curves in the figures for relatively large droplets with initial size 60 μm in Flames 1 and 4 and 65 and 75 μm in Flames 2 and 3, respectively. These initial sizes are critical since they represent the maximum size of droplets that at the prevailing conditions and for the specified initial position fully vaporized before punching through the flame. Since the behavior is monotonic, the implication is that any droplet larger than these critical ones starting at the same position survived the flame and burned on the oxidizer side, isolated from the cloud. Since evidence of this phenomenon was offered experimentally by the streaks discussed in connection with Fig. 2, we can attempt to correlate these findings, as elaborated below.

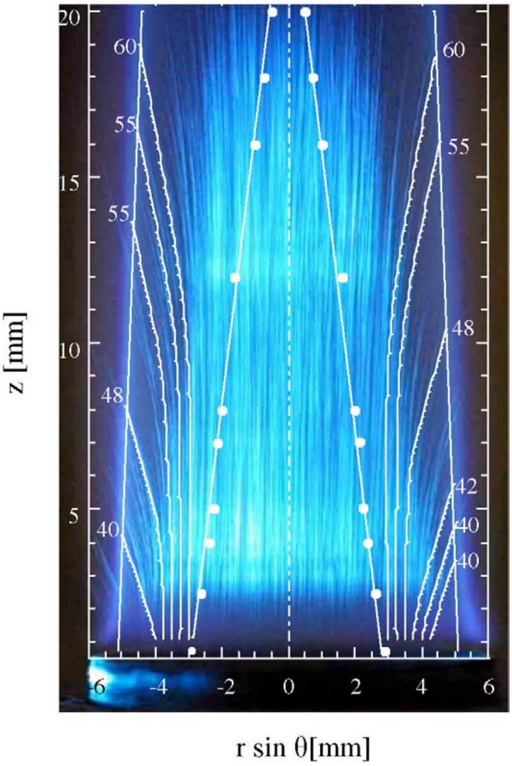

Fig. 11. Trajectories of the $\mathrm{Da_V} = 1$ droplets for Flame 1. Numbers on individual trajectories are the initial sizes of the droplets. Also shown in the figure are four oblique lines, the two outermost corresponding to the flame position, the two innermost to the boundary of the cold region. Trajectories are superimposed on a long exposure laser light scattering image. Clearly visible, near the base, are trajectories of droplets surviving the flame.

3.5. Vaporization Damköhler number

The phenomenon of droplets punching through the flames and burning on the oxidizer side in an internal combustion mode can be rationalized in terms of a comparison of two characteristic times, an evaporation time and the droplet residence time in the high-temperature vaporizing part of the flame. Their ratio is a vaporization Damköhler number [22] defined as $\mathrm{Da_V} = \frac{\bar{K}}{d_0^2}\frac{s}{\bar{w}}$, where s is the radial width of the vaporizing region and $\bar{w}$ is the average velocity of the droplet normal to the reacting layer. The case of $\mathrm{Da_V} = 1$ corresponds to those trajectories computed for the largest initial droplet size in Fig. 10 and is critical since it separates two different classes of droplets. The first class is composed of droplets (e.g., 33 and 40 µm in Figs. 10a and 10b) with $\mathrm{Da_V} > 1$ that completely vaporized inside the flame. The other class consists of droplets for which $\mathrm{Da_V} < 1$. They survived the diffusion flame and burned isolated on the outside.

Figs. 11–14 report conditions of $\mathrm{Da_V} = 1$ for different initial radial positions for all flames, with Figs. 11 and 13 adapted from [7] for comparison purposes. In each figure we can identify: two oblique lines close to the centerline, marking the outer edge of the cold core of the flames, where no evaporation occurred; two outermost either oblique or nearly vertical lines, that corresponded with the flame location, as inferred from the location of peak temperature measurements; and a number of trajectories for which the condition $\mathrm{Da_V} = 1$ applied, each trajectory being labeled with a number representing the initial diameter of the trajectory droplet. The critical diameter can be determined as $d_{\mathrm{crit}} = (\bar{K}\frac{s}{\bar{w}})^{0.5}$. If we assume that all the droplets that reached the flame had an equal average vaporization constant, since they had a similar temperature history, the critical diameter will be function only of the residence time in the flame. Generally, droplets exiting the duct near the tube wall had a smaller path to the flame, which implies low residence time in the vaporization region and small critical diameters. Vice versa, droplets that exited the duct closer to the center had a longer vaporization time because of the large pathway to the flame. As a result, the critical diameters were larger. By the same token, for given trajectories corresponding to a critical diameter, if a droplet of that diameter exited the fuel tube at a large radial position, it would punch through the flame.

A laser light-scattering image taken in the lower part (0–17 mm) of Flame 1 is also shown in Fig. 11. Trajectories of the droplets in an axial plane illuminated by the laser are visible. The 0.05-s exposure time evidences the entire droplet trajectories. Although the frequency of droplets crossing the flame decreased with height, droplets can be seen crossing the reacting layer at a height well above the limit of the luminous streaks of Fig. 2a.

Flame 2 (Fig. 12) exhibited a reaction layer that was not quasi-vertical, unlike Flame 1, but approached a right circular cone. This affected the thickness of the vaporization region and implies that the critical diameter was not only a function of the radial coordinate of the droplet at $z = 0$, but also of the height at which the droplets exited the flame and, as a consequence, of the vertical velocity. Clearly noticeable, when Fig. 11a is compared with Fig. 12, is the increased critical diameter for comparable heights in the flame. At first, it should be noticed that their cold regions evolved similarly because of the equal Peclet number between the two flames. But, because of the different flame shapes, the vaporization region was larger at atmospheric pressure. The wider vaporization region should have resulted in smaller droplets punching through. But two effects combined to overcome the decrease in path length. First, Flame 1 had

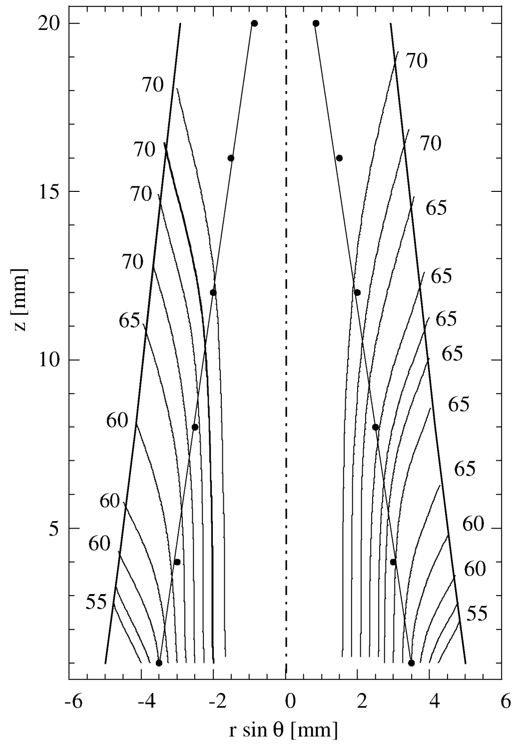

Fig. 12. Trajectories of the $\mathrm{Da_V} = 1$ droplets for Flame 2. See legend of Fig. 11.

typical radial velocities approximately 50% higher than Flame 2; and, second, the average temperature along the path was 10% larger in Flame 2.

In the case of Flame 3, in Fig. 13, as previously remarked, because of Peclet number effects, the high-temperature region was even narrower, as compared to Flames 1 and 2. For the same axial position, the critical diameters were larger than for Flame 1. Since the path to the flame was shorter, one would expect lower values of the critical diameter. Again, two effects offset the decrease in path length. First, the average vaporization constant increased because of the increased maximum temperature (see Fig. 9); second, the average radial velocity was lower in the high-pressure case, as shown in Fig. 7.

In Fig. 14, corresponding to Flame 4, because of buoyancy-driven instabilities, only the first 16 mm of the flame are characterized. The Peclet number was the same as for Flame 3, and the cold regions in the two flames was similar. Outside this region, axial and radial velocities had comparable values. Thus, the droplet trajectories were curved more than in other cases. For comparable heights, the vaporization region was narrower than all other cases, but the velocity at which the droplets approached the flame was lower. The final residence time increased, as did the critical droplet size.

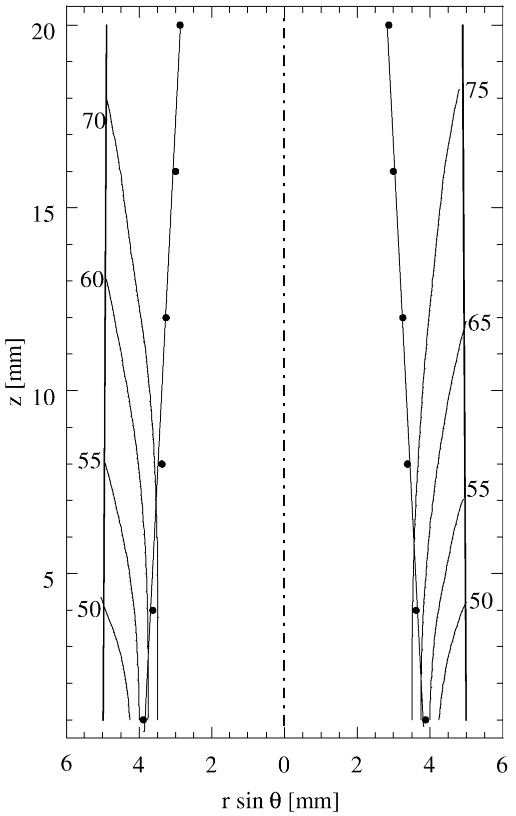

Fig. 13. Trajectories of the $\mathrm{Da_V} = 1$ droplets for Flame 3. See legend of Fig. 11.

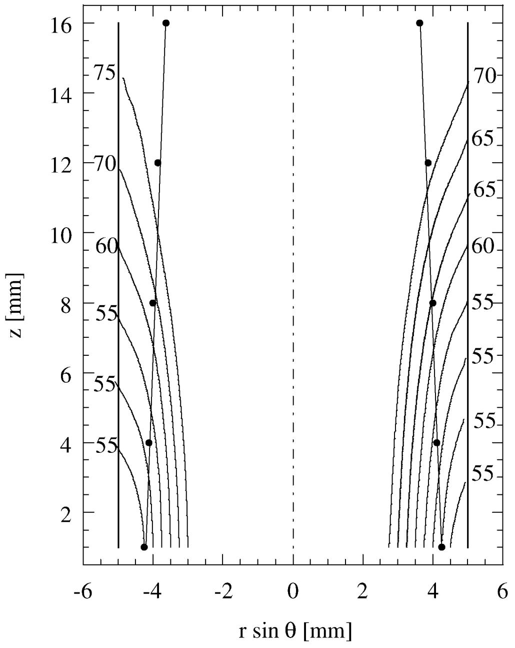

Fig. 14. Trajectories of the $\mathrm{Da_V} = 1$ droplets for Flame 4. See legend of Fig. 11.

The results in Figs. 11–14 are consistent with the visual appearance of the flames. At lower axial positions the critical diameters were smaller and many droplets of the initial distribution survived the diffusion flame eventually igniting on the outside. A comparison of the critical diameters with the initial size distribution shows that some droplets eventually reached the diffusion flame also at position relatively far away from the duct. These droplets did not always ignite outside of the reacting layer since their diameter was greatly reduced with respect to the initial value and might have been below the extinction value [23]. Moreover, the thickness of the region of low oxidizer concentration outside the reacting layer increased with height, making the ignition process more difficult.

This finding is also consistent with Fig. 11, where droplets exiting the flame were seen above the limit of luminous streaks. A different behavior is seen in Flame 4, where luminous streaks appeared also at relatively high axial positions. Two effects contributed to this phenomenon. First, the critical diameter for droplet flame extinction decreases inversely with the pressure [23]. Therefore, small droplets could still burn. Second, the initial distribution in the case of Flame 4 (Figs. 3d and 3e) presented a larger percentage of droplets above 80 μm. As a result, more droplets could punch through the flame.

Clearly, because of the average radial velocity changes at different pressures, the critical diameter could not be correlated to the boundary layer thickness, and, therefore, to the Peclet number, as we first assumed in the initial design of the experiment.

4. Conclusions

An experimental study was conducted on high-pressure laminar spray diffusion flames in the 0.1–0.9 MPa pressure range. Buoyancy driven instabilities were a major difficulty in establishing such flames. The addition of an extra chamber to the experimental apparatus to act as a dead volume in the post-flame region proved successful in delaying the onset of the instabilities and allowing for the establishment of steady flames.

The flames were stabilized in a coflow configuration, with high dilution of argon on the fuel side and pure oxygen on the oxidizer side. All flames presented a cold inner core, in which little or no vaporization took place, surrounded by an envelope flame buried in a thermal boundary layer, where most of the droplet evaporation occurred. Some droplets survived the common envelope flame and burned isolated on the oxidizer side, in a mixed regime of internal/external group combustion. Evidence of this behavior was provided photographically by the presence of streaks associated with individual droplets burning, especially near the base of the flame. It was also confirmed by a detailed physical characterization of the flames, through the measurements of droplet and gaseous velocity components and gas temperature. Such measurements allowed for the reconstruction of the entire vaporization history and lead to the establishment of a criterion for droplet survival beyond the envelope flame, based on the critical value of a suitably defined vaporization Damköhler number. Droplets, whose vaporization Damköhler number was smaller than unity, outlived the envelope flame and burned isolated on the outside, while droplets having vaporization Damköhler larger than unity fully vaporized before reaching the flame.

The scaling and self-similar behavior of the flames was investigated and pointed to a mixed regime, with a momentum-controlled cold core and a buoyancy-controlled high-temperature boundary layer, the thickness of which varied significantly with pressure, as expected from Peclet number scaling. At pressures above the atmospheric, because of the decrease in thermal diffusivity, the growth of this layer was reduced, as was the thickness of this vaporization region.

Acknowledgments

The support of NSF, Grant CTS-9904296 (Dr. Farley Fisher, Contract Monitor), is gratefully acknowledged. The authors thank Professor Amable Liñàn for helpful discussions on flame scaling.

Appendix A

It is well known that in laminar flames buoyancy induces instabilities with a characteristic frequency between 10 and 20 Hz [13,14,16]. Those instabilities build up as a function of height, and appear only in buoyant flames that are sufficiently tall, that is, in flames in which there is sufficient time for the instabilities to develop. It is worth remarking that also in flames smaller than the minimum height for the flickering to appear the hot gases above the flame tip might be subject to these oscillations. In unconfined environments such fluctuations above the flame are not visible and are irrelevant since they do not affect the reacting part. In a closed vessel, in contrast, any fluctuation anywhere in the vessel can affect the reacting layer.

A simple analogy between fluid dynamics and electric circuits is helpful in understanding how in a closed vessel the buoyancy-induced instabilities can

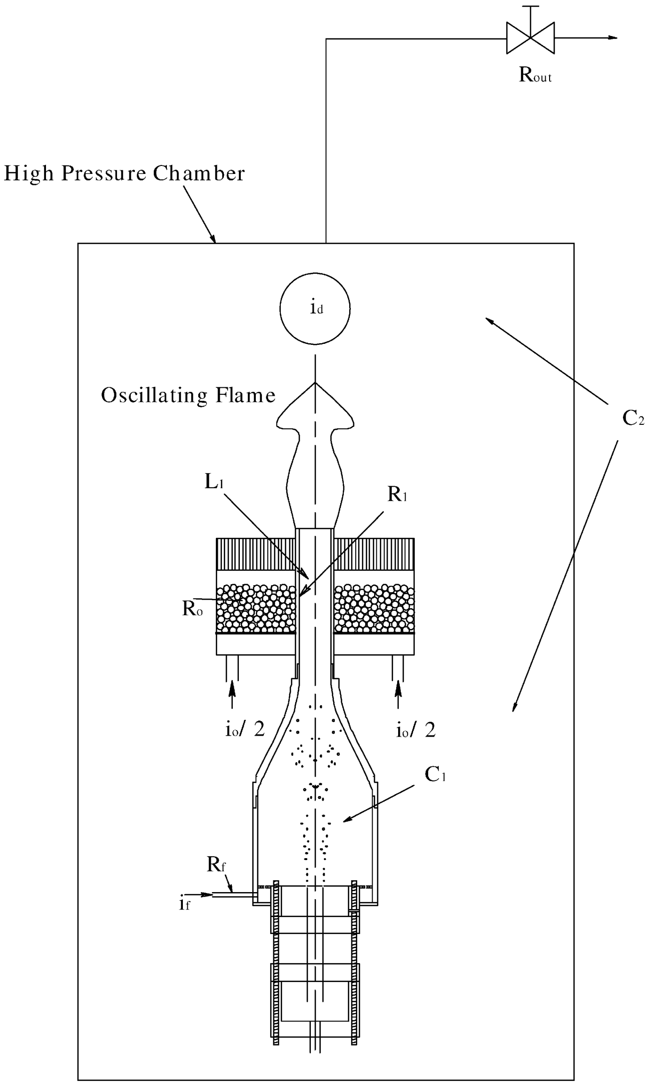

Fig. A.1. Combustion chamber schematic with electric circuit components for the electroacoustic analogy.

affect a flame and in finding suitable remedies to them. A gaseous flow can be treated as the analogue of electric current, a volume becomes a capacitor, flow resistance yielding a pressure drop is the equivalent of a resistor, and pressure corresponds to voltage. A complete treatment of the electroacoustic analogy is reported in [24].

In Fig. A.1 we can see a schematic of the burner inside the high-pressure vessel, while in Fig. A.2 the analog electric circuit is represented. i_F is the incoming flow of fuel and inert gas, i_o the flow of oxidizer, with R_f and R_o being the resistance along the fuel and oxidizer lines, respectively. The valve at the exit of the vessel is the output resistor R_{out} and the straight duct connecting the main volume of the burner with the flame region is represented by a resistor R_1. C_1 is the volume of the atomization chamber and C_2 is volume available for the gases inside the vessel. R_2 represents the pressure drop met by the gas inside the vessel, in the movement towards the source of instabilities. The instability of the hot gases is modeled as a periodic current i_d with zero average (no source of mass). It is interesting to notice that the couple C_1, R_1 acts as a low-pass filter for i_d, while C_1 and R_f act as a low-pass filter for i_f that is not affected by the instabilities because of the high value of R_f, which determines a very low cutoff frequency ($f = \frac{1}{2}\pi R_f C_1$).

i_d, the analogue of the buoyancy-generated instability, acts in the region of hot gases above the flame at a position here labeled F. Applying Kirchhoff's first law at the node F we obtain

$$i_{\mathrm{d}} = i_1 + i_2 - i_{\mathrm{OUT}} + i_{\mathrm{o}}.$$

The currents flowing in the circuit can be divided into two components: a DC component, here represented in capital letters, and a small AC component, superimposed on the continuous one. Thus,

$$i_1(t) = I_1 + i_{\mathrm{I}}(t),$$

$$i_{\mathrm{O}}(t) = I_{\mathrm{O}} + i_{\mathrm{o}}(t),$$

$$i_2(t) = I_2 + i_{\mathrm{II}}(t),$$

$$i_{\mathrm{OUT}}(t) = I_{\mathrm{OUT}} + i_{\mathrm{out}}(t).$$

The application of Kirchhoff's first law at the B node results in

$$i_1(t) = I_{\mathrm{F}} + i_{\mathrm{c}}(t),$$

where $I_{\mathrm{F}} = i_{\mathrm{f}}$ is constant in time because of the previously discussed filtering effect of R_{f}, and i_{c} has only an AC component due to presence of C_1. The balance at node F can be rewritten as

$$i_{\mathrm{d}}(t) = I_{\mathrm{F}} + I_{\mathrm{O}} + I_2 - I_{\mathrm{OUT}} + i_{\mathrm{c}}(t) + i_{\mathrm{o}}(t) + i_{\mathrm{II}}(t) - i_{\mathrm{out}}(t),$$

where $I_2 = 0$ because of the capacitor C_2. We shall now solve the electric circuit using the small-signal approximation and separate the AC component from the small periodic oscillation. The DC component can be written as

$$I_{\mathrm{F}} + I_{\mathrm{O}} = I_{\mathrm{OUT}},$$

which represents the global mass balance fuel + oxidizer = products. This result follows from the fact that buoyancy is not a source of mass and, consequently, it does not affect the total mass balance.

The circuit for the small signal analysis is shown in Fig. A.2b. It can be solved in terms of the complex impedance $Z = R + j(\omega L - \frac{1}{\omega C})$. Next, we assume that $R_{\mathrm{out}} \gg R_1$, $R_{\mathrm{out}} \gg R_2$, and $R_{\mathrm{o}} \gg R_1$, $R_{\mathrm{o}} \gg R_2$ which, from a fluid dynamic point of view, is equivalent to assuming that the pressure drop of the exit valve and the pressure drop along the oxygen supply line are much larger than the pressure drop along the burner duct and the resistance met by the fluid in the chamber in its motion towards the source of instabilities. The circuit for the signal component reduces to the one in Fig. A.2c with $Z_1 = R_1 - j\frac{1}{\omega C_1}$, $Z_2 = R_2 - j\frac{1}{\omega C_2}$, and $i_{\mathrm{d}} = i_{\mathrm{c}} + i_{\mathrm{II}} = \frac{V}{Z_1} + \frac{V}{Z_2}$.

The objective is to reduce the fluctuations in the fuel flow rate or i_{c}. If $i_{\mathrm{c}}(t) \neq 0$, fluctuations in the fuel flow at the top of the burner occur and flame flickering ensues. The flickering is strictly dependent on the presence of the high-pressure chamber. If the flame were in open air, that is, with $R_2 = 0$ and $C_2 = \infty$, i_{d} would be completely absorbed by C_2 without affecting i_1. The effect of i_{c} is analogous to the classic buoyancy induced instabilities on the flame.

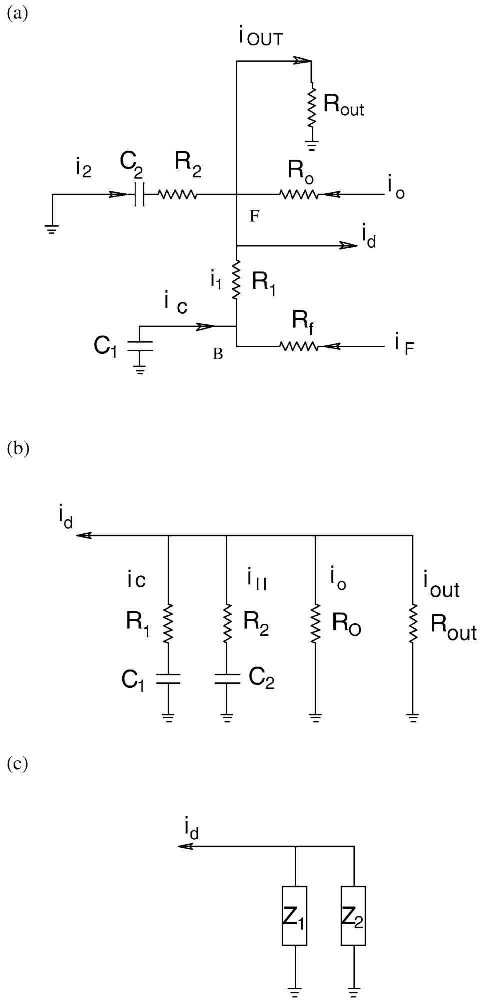

Fig. A.2. (a) Analog electric circuit; (b), (c) circuits in the small-signal limit.

Since the magnitude of the disturbance $|i_{\mathrm{d}}|$ is fixed, once the source, that is, the flame, is fixed, one has to maximize the current i_{II} in order to reduce the value of i_{c}. This can be done by increasing either the capacity C_2 or the resistance R_1 or by reducing the capacity C_1. The components R_1 and C_1 are related to the atomizer design. Even a substantial redesign of the atomizer in the light of these new constraints would not allow for a critical reduction of the instabilities. To achieve a one-order-of-magnitude reduction of the fluctuations the only plausible way is to increase the capacitor C_2 by adding an extra chamber, to act as a dead volume. An extra duct, measuring approximately 190 cm in length and 8.2 cm in diameter, was added above the optically accessible section, as shown in Fig. 1. The total length of the system reached 240 cm for a total volume of 12,700 cm^3, approximately 1000 times larger than the burner volume.

The use of a Helmoltz resonator [24] would have the same damping effect without requiring an excessive increase in the volume of the experimental apparatus. This possibility, although very appealing, had to be discarded since preliminary results with gaseous flames showed that as the pressure increased from 1 to 8 atm the fluctuation frequency changed from 11 to 20 Hz, which would impose the need for an impractical tunable Helmoltz resonator.

References

[1] S.D. Givler, J. Abrahaman, Prog. Energy Combust. Sci. 22 (1996) 1.
[2] S.C. Li, P.A. Libby, F.A. Williams, Proc. Combust. Inst. 24 (1992) 1503.
[3] G. Chen, A. Gomez, in: K. Kuo (Ed.), Recent Advances in Spray Combustion: Measurements and Model Simulation, vol. II, AIAA, Reston, VA, 1996, pp. 187–199.
[4] H.H. Chiu, T.M. Liu, Combust. Sci. Technol. 17 (1977) 127.
[5] H.H. Chiu, H.Y. Kim, E.J. Croke, Proc. Combust. Inst. 19 (1982) 971.
[6] F.V. Bracco, Combust. Sci. Technol. 8 (1973) 69.
[7] S. Russo, A. Gomez, Proc. Combust. Inst. 29 (2002) 601.
[8] S. Russo, Ph.D. thesis, Department of Mechanical Engineering, Yale University, New Haven, CT, 2002.
[9] L.P. Gao, Y. D'Angelo, I. Silverman, A. Gomez, M.D. Smooke, Proc. Combust. Inst. 26 (1996) 1739.
[10] A.N. Karpetis, A. Gomez, J. Fluid Mech. 397 (1999) 231.
[11] A.M. Gañán-Calvo, Phys. Rev. Lett. 80 (2) (1998) 285.
[12] V. Vilimpoc, L.P. Goss, Proc. Combust. Inst. 22 (1988) 1907.
[13] R.W. Davis, E.F. Moore, W.M. Roquemore, L.-D. Chen, V. Vilimpoc, L.P. Goss, Combust. Flame 83 (1991) 263.
[14] T.W. Park, S.K. Aggararwal, V.R. Katta, Combust. Flame 99 (1994) 767.
[15] T. Kadota, H. Hiroyasu, A. Farazandehmehr, Combust. Flame 29 (1977) 67.
[16] H. Sato, K. Amagai, M. Arai, Combust. Flame 123 (2000) 107.
[17] A. Gomez, I. Glassman, Proc. Combust. Inst. 21 (1986) 1087.
[18] G. Sugiyama, Proc. Combust. Inst. 25 (1994) 601.
[19] L. Talbot, R.K. Cheng, R.W. Schefer, D.R. Willis, J. Fluid. Mech. 101 (1980) 737.
[20] Synergy Software, Kaleidagraph Reference Guide, Reading, PA, 1996.
[21] I. Glassman, Combustion, third ed., Academic Press, San Diego, CA, 1996.
[22] J.B. Greenberg, Combust. Flame 77 (1991) 229.
[23] X. Wu, C.K. Law, C. Fernandez-Pello, Combust. Flame 44 (1982) 113.
[24] L.L. Beranek, Acoustics, McGraw–Hill, New York, 1954.